CFA-14 – a perfluorinated metal–organic framework with linear 1-D Co^{II}-chains showing temperature dependent spin-chain magnetic ordering†

J. Fritzsche,[a] M. Grzywa,[a] D. Denysenko,[a] S. Reschke,[b] K. Sugimoto,[c] H.-A. Krug von Nidda,[b] D. Schmidtner[a] and D. Volkmer*[a]

The synthesis and crystal structure of the perfluorinated metal–organic framework (MOF) **CFA-14** (Coordination Framework Augsburg University-14), Co^{II}_2(tfpb)$(OH)_2$ (H_2-tfpb = 1,4-bis(3,5-bis(trifluoromethyl)-1*H*-pyrazole-4-yl)benzene) are described. The cobalt-containing MOF crystallizes in the tetragonal crystal system within the space group $I4_1/acd$ (no. 142) and the unit cell parameters are as follows: a = 20.3213(11) Å, c = 12.4045(8) Å, V = 5122.5(6) Å^3. **CFA-14** features a porous two-fold interpenetrated 3-D microporous structure constructed from 1-D chains of cobalt(II) ions expanding in the c-direction, bridged by OH^- groups and $tfpb^{2-}$ ligands. The structure exhibits quadratic channels running along the c-axis. **CFA-14** is fully characterized by synchrotron single crystal X-ray diffraction, thermogravimetric analysis, variable temperature powder X-ray diffraction, IR- and UV-Vis spectroscopy, photoluminescence and gas sorption measurements. Moreover, the magnetic properties of **CFA-14** are examined *via* SQUID measurements.

Introduction

Due to their extraordinary chemical and physical properties such as enhanced thermal and chemical stability, low surface energy and surface tension, strong hydrophobicity and good stability against (self-)oxidation and photonic decomposition, fluorous metal–organic frameworks (FMOFs) have attracted huge interest during the last few years.[1] Replacing hydrogen atoms by fluorine atoms within an organic linker often leads to completely new and unexpected coordination geometries within metal–organic frameworks caused by steric hindrance due to the larger size of CF_3-groups compared to CH_3-groups or simple hydrogen atoms.

The combination of pyrazolate (pz) based ligands with copper ions often leads to the formation of polynuclear secondary building units (SBUs), for example tri- or tetranuclear (planar) $[Cu^I_3(pz)_3]$ or $[Cu^I_4(pz)_4]$ units that are well known in literature.[2] In contrast to these "simple" coordination geometries, fluorinated pyrazolate ligands show quite complex and unexpected coordination with copper ions. We recently reported on the pyrazolate-based copper MOFs **M[CFA-4]** (M = Cu, K, Cs, Ca),[3] which is built up from a pentanuclear $[Cu^I_5(pz)_6]^-$ SBU, and **M[CFA-13]**,[4] containing trinuclear $[Cu^I_3(pz)_4]^-$ SBUs as well as Cu(II) paddle-wheel SBUs. Both MOFs have negatively charged lattices and free cations in the pores that provide charge neutralisation.

The cobalt(II)-containing pyrazolate frameworks **MFU-1** and **MFU-2** are both constructed from the non-fluorinated organic ligand 1,4-bis[(3,5-dimethyl)-1*H*-pyrazole-4-yl]benzene (H_2-bdpb) but with different reaction conditions.[5] **MFU-1** forms a structural analogue of the Zn-containing **MOF-5** [6] with oxo-centred tetranuclear $\{Co_4O\}$ cores, whereas **MFU-2** contains cross-linked 1D cobalt(II) chains.

Replacing the methyl groups in the H_2-bdpb ligand by trifluoromethyl groups leads to the ligand 1,4-bis(3,5-bis(trifluoromethyl)-1*H*-pyrazole-4-yl)benzene (H_2-tfpb) that forms the stable cobalt(II)-MOF **CFA-14**. Although there are some similarities between the structures of **MFU-2** and **CFA-14**, the MOFs are not isostructural due to the steric limitations introduced with the altered fluorinated organic ligand.

[a]*Augsburg University, Institute of Physics, Chair of Solid State and Materials Chemistry, Universitaetsstrasse 1, 86159 Augsburg, Germany. E-mail: dirk.volkmer@physik.uni-augsburg.de; Fax: +49 (0)821 598 5955; Tel: +49 (0)821598 3006*

[b]*Augsburg University, Institute of Physics, Chair of Experimental Physics V, Center for Electronic Correlations and Magnetism, Universitaetsstrasse 1, 86159 Augsburg, Germany*

[c]*Japan Synchrotron Radiation Research Institute, Research & Utilization Division, 1-1-1 Kouto, Sayo-cho, Sayo-gun, Hyogo, Japan*

† Electronic supplementary information (ESI) available: Crystallographic data, IR- and DRIFT-IR and gas sorption measurements for **CFA-14**. CCDC 1811523. For ESI and crystallographic data in CIF or other electronic format see DOI: 10.1039/c8dt02841a

In this paper we present the synthesis of the novel cobalt(II)-based metal–organic framework **CFA-14** from the fluorinated organic ligand H_2-tfpb and cobalt nitrate and the respective characterization. The crystal structure of **CFA-14** was determined by synchrotron single crystal X-ray diffraction. Besides the structure solution, **CFA-14** was characterized by thermogravimetric analysis, variable temperature X-ray diffraction, IR- and UV-Vis spectroscopy, photoluminescence and gas sorption measurements. Furthermore, magnetic susceptibility measurements were performed to investigate the magnetic properties of **CFA-14**.

Results and discussion

Synthesis and characterisation

The ligand 1,4-bis(3,5-bis(trifluoromethyl)-1*H*-pyrazole-4-yl) benzene (H_2-tfpb) was synthesized *via* Suzuki-coupling reaction according to recently published procedure.[3]

CFA-14 framework was obtained as purple block crystals after heating a solution of H_2-tfpb ligand and cobalt(II) nitrate hexahydrate at 120 °C in MeOH in the presence of 2,6-lutidine (Scheme 1). Standard solvothermal synthesis procedure leads to strongly adhered acicular crystals (Fig. 1a and b).

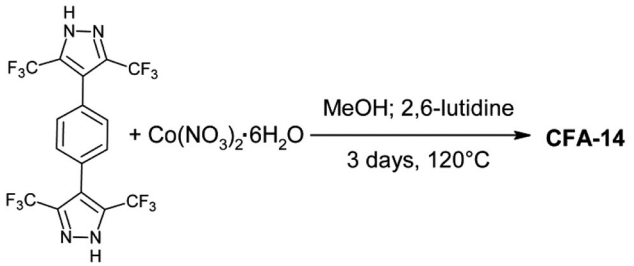

Scheme 1 Synthesis of **CFA-14** from the H_2-tfpb ligand and cobalt(II) nitrate.

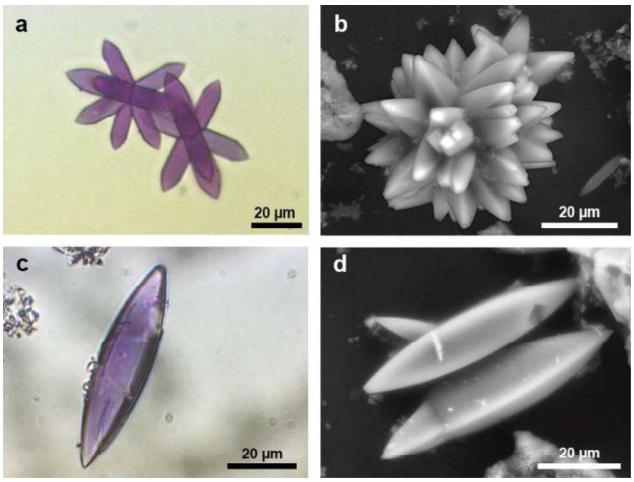

Fig. 1 **CFA-14**: Optical micrographs (a, c); SEM images (b, d).

Optimising the reaction conditions by heating at a constant rate of 0.2 °C per minute up to 120 °C leads to separated single crystals with a length of up to 35 µm (Fig. 1c and d).

Single crystal structure analysis

A synchrotron single X-ray diffraction study revealed that **CFA-14** crystallizes in the tetragonal crystal system within the space group $I4_1/acd$ (no. 142). The asymmetric unit consists of one cobalt, one nitrogen, one oxygen, two hydrogen, three fluorine and five carbon atoms. An ORTEP-style plot of the asymmetric unit of **CFA-14** is shown in the ESI, Fig. S6.† The atomic coordinates and anisotropic displacement parameters, bond lengths and angles are presented in the ESI (Tables S1–S3†).

CFA-14 features a two-fold interpenetrated 3-D microporous structure constructed from 1-D chains of cobalt(II) ions expanding in the *c*-direction bridged by OH^- groups and $tfpb^{2-}$ ligands (see Fig. 2). Each Co(II)-ion placed on an axis of 2-fold symmetry is tetrahedrally coordinated by two nitrogen and two oxygen atoms stemming from two different $tfpb^{2-}$ ligands and two different OH groups, respectively. The OH^- groups in the chains are oppositely positioned to the $tfpb^{2-}$ ligands. The structure exhibits quadratic channels running along the *c*-axis. These square channels in **CFA-14** have apertures of 4.6 Å (distance between opposed pyrazol rings of the $tfpb^{2-}$ ligands taking the van der Waals radii of 1.7 Å for the carbon atoms into account). The distance between Co(II)-ions and N-donor atoms is equal to 2.015(7) Å, whereas the distance between Co(II)-ions and O-donor atoms is 1.910(6) Å. The Co···Co distance between adjacent cobalt(II)-centres is 3.198(2) Å. These values are in good agreement with those found in similar compounds.[5,7] Interestingly, a related structure to **CFA-14** constructed from 1D chains of cobalt(II)-ions and 1,4-bis[(3,5-dimethyl)pyrazol-4-yl] ligands (**MFU-2**) has been reported earlier by us.[5] The Co(II)-ions in **MFU-2** are also tetrahedrally coordinated, but in contrast to the **CFA-14** structure, Co(II)-ions in **MFU-2** are only coordinated by N-donor atoms stemming from four different $bdpb^{2-}$ ligands and no bridging OH^- groups are present in the structure. Moreover, contrary to **CFA-14**, **MFU-2** exhibits a non-interpenetrated microporous structure. Similar to **CFA-14**, **MFU-2** shows quadratic channels with apertures of 6.4 Å (distance between opposed phenyl rings assuming van der Waals radii of 1.7 Å for the carbon atoms) running along the *c*-axis. A calculation using the SQUEEZE[8] software reveals that the initial solvent accessible void volume in **CFA-14** is 1255 $Å^3$, which is 24.5% of the unit cell volume 5122.5(6) $Å^3$.

Thermal analysis and VTXRPD studies

Thermal and structural stability of **CFA-14** were determined from TGA and VTXRPD measurements. To remove the occluded solvent molecules, the sample was dried in vacuum at 100 °C for 4 h prior to TGA measurements. As shown in Fig. 3, **CFA-14** is stable up to almost 300 °C, since the thermogravimetric profile under nitrogen exhibits no weight loss step. The beginning weight loss above 300 °C is due to gradual decomposition of the framework.

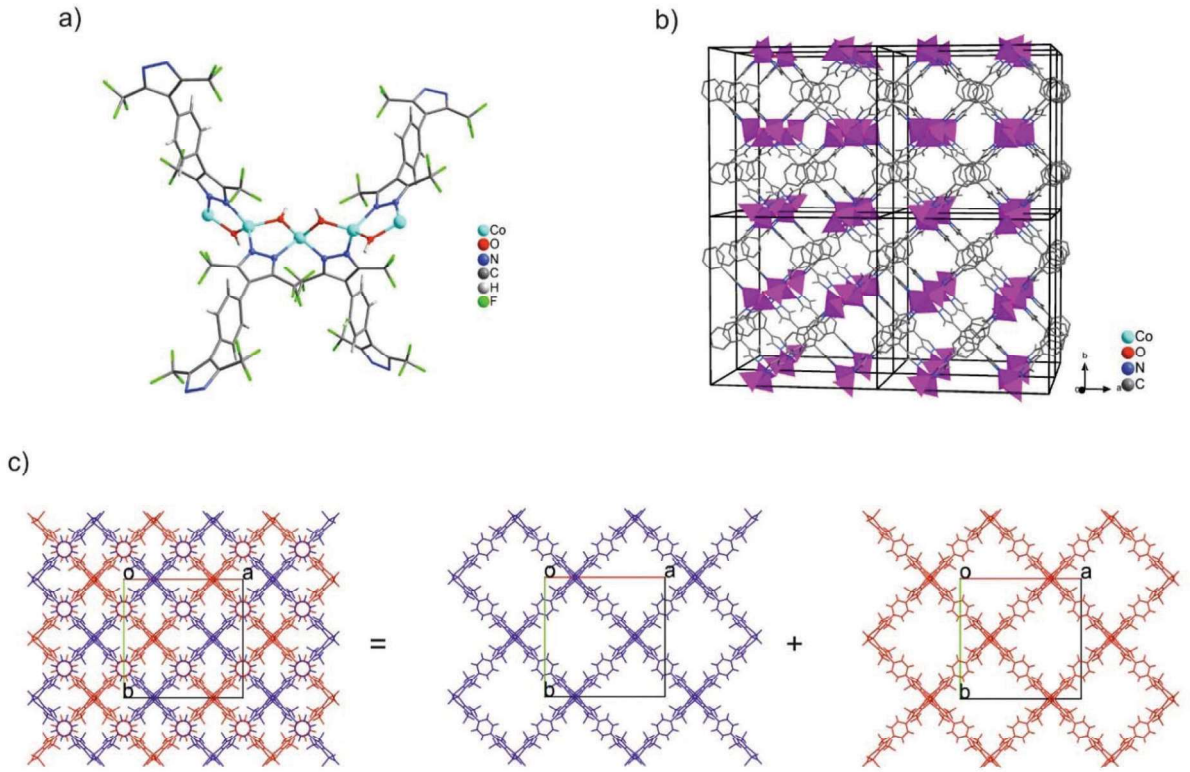

Fig. 2 (a) Portion of the crystal structure of **CFA-14** emphasizing the coordination environment of cobalt(II)-ions. (b) Crystal packing diagram of **CFA-14** showing 1D chains of cobalt(II)-ions expanding in the *c*-direction. Fluorine and hydrogen atoms have been omitted for clarity. (c) Packing diagram of **CFA-14** showing the two-fold interpenetrated microporous 3D framework. View in *c*-direction.

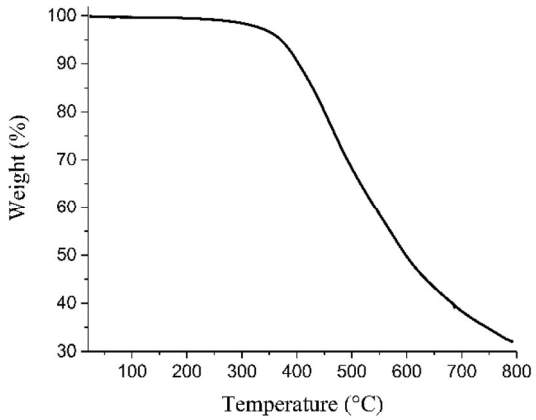

Fig. 3 Temperature dependent weight loss of **CFA-14** under nitrogen flow.

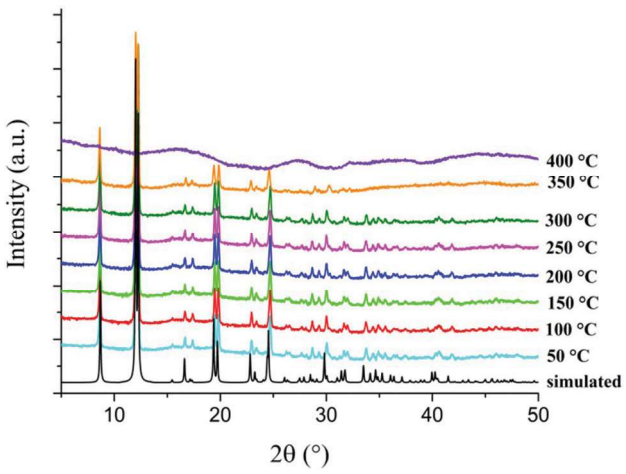

Fig. 4 VTXRPD plots of **CFA-14** in the range of 50–400 °C. The black XRPD pattern is simulated based on single crystal X-ray data.

Phase purity of **CFA-14** was confirmed by XRPD measurements (Fig. 4). The experimental XRPD pattern is consistent with the one calculated from the single crystal structural data (see black curve in Fig. 4). Differences in peak intensities can be explained by occluded solvent molecules in the synthesized MOF. Variable temperature X-ray powder diffraction studies of **CFA-14** are in good agreement with the results from the TGA measurement, showing that the framework is stable up to 300 °C (Fig. 4). Above this temperature the intensity of the peaks at higher 2θ values decreases, giving a first indication that the long range order within the crystal structure likewise decreases. Crystallinity is completely lost above 350 °C. The unit cell parameters of **CFA-14** dried at room temperature were determined using the DICVOL and TREOR 90 software[9] based on the powder pattern collected at room temperature. Both

programs determined a quite similar tetragonal cell that is in good agreement with the solution from the single crystal measurement and shows the following cell parameters: $a = b =$ 20.391 Å, c = 12.434 Å, V = 5170 Å^3 (TREOR, M_{20} = 19, F_{20} = 35 (0.005304, 109)) and $a = b$ = 20.377 Å, c = 12.432 Å, V = 5162 Å^3 (DICVOL, M_{20} = 19.2, F_{20} = 36.7 (0.0053, 103)). $I4_1/acd$ is proposed as a possible space group, which is identical with the one determined from the single crystal measurement.

Gas sorption measurements

Argon gas sorption measurements on **CFA-14** at 77 K confirm permanent porosity of the structure. Prior to the measurement, the sample of **CFA-14** was washed with methanol and heated at 200 °C in high vacuum for 18 hours to remove occluded solvent molecules. The resulting argon adsorption/desorption isotherm follows type I behaviour, which is characteristic for microporous solids. The maximum uptake achieved at 77 K and p/p_0 = 0.99 is 193 cm^3 g^{-1} (Fig. 5), corresponding to a total pore volume of 0.24 cm^3 g^{-1}, respectively. The micropore volume of **CFA-14** determined at p/p_0 = 0.2 is 0.20 cm^3 g^{-1} which corresponds well to the value calculated from the crystal structure data. The BET surface area determined in the range p/p_0 = 0.003–0.03 is 567 m^2 g^{-1}. To evaluate the pore size distribution of the **CFA-14** framework, the argon sorption isotherms sampled for **CFA-14** at 77 K were analysed using non-local density functional theory (NLDFT)[10] implementing a carbon equilibrium transition kernel for argon adsorption based on a slit-pore model.[11] The distribution calculated by fitting the adsorption data reveals two well-defined micropores with diameters of 5.5 Å and 9.8 Å (Fig. 5, inset).

The isosteric heat of CO_2 adsorption for **CFA-14** determined from adsorption isotherms measured in the temperature range of 223–273 K (see ESI, Fig. S7†) reaches a value of almost 32 kJ mol^{-1} at low loading (<0.5 mmol g^{-1}) (see Fig. 6). The isosteric heat of CO_2 adsorption in MOFs typically ranges from

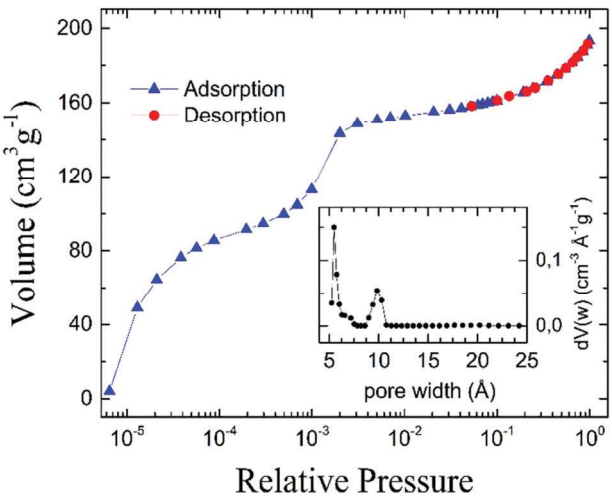

Fig. 5 Argon adsorption (blue) and desorption (red) isotherms of **CFA-14** at 77 K. Inset: Pore size distribution calculated from these isotherms.

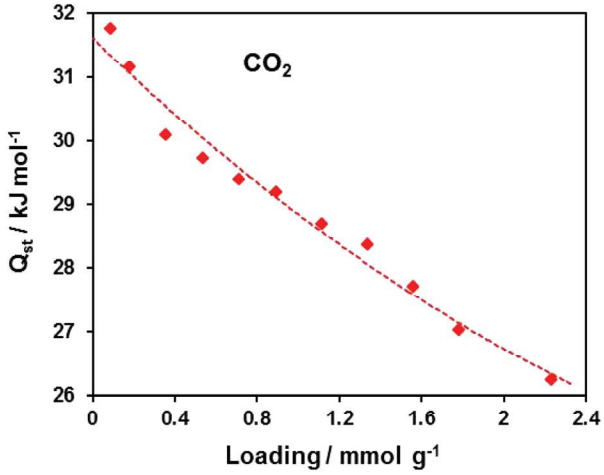

Fig. 6 Isosteric heat of CO_2 adsorption in **CFA-14**.

25–35 kJ mol^{-1},[12] in exceptional cases a value of up to 90–96 kJ mol^{-1} can be reached.[13]

To explore whether the adsorption of CO_2 in **CFA-14** is due to either physical interactions or chemisorption, CO_2 gas sorption on **CFA-14** was studied by diffuse reflectance Fourier-transform IR spectroscopy (DRIFT) (see ESI Fig. S2–S5†). First, the sample was heated up to 150 °C under nitrogen flow. After cooling down to room temperature, a FT-IR spectrum of the activated **CFA-14** was recorded under nitrogen. The gas flow was subsequently switched to CO_2 and another spectrum was recorded. The temperature was then gradually decreased in 20 °C steps down to −60 °C. At this temperature the gas flow was changed to nitrogen again. The DFT calculated vibration frequencies for free CO_2 gas are 2366 cm^{-1}, 1318 cm^{-1} and 637 cm^{-1},[14] the experimental measured bands can be slightly shifted. Chemical bonding of CO_2 to the bridging OH^- groups within the structure of **CFA-14** would lead to the formation of hydrogen carbonate. Hydrogen carbonate species known from literature show IR bands in the region of ~1650 cm^{-1}, ~1400–1500 cm^{-1} and ~1200 cm^{-1}.[15] The DRIFT IR-spectrum of **CFA-14** shows no bands that can be attributed to hydrogen carbonate species as only bands of free CO_2 gas can be observed. Hence, there are solely physical interactions between CO_2 and the MOF but no chemisorption. We expect that cobalt centres as well as the OH^- bridges within **CFA-14** are well shielded by the CF_3 groups of the ligand and, therefore, are both not freely accessible. As a consequence, chemical binding of small molecules to **CFA-14** is not possible.

Magnetic properties

To investigate the magnetic properties of **CFA-14**, the magnetization M was measured for a polycrystalline sample in magnetic fields of H = 1, 10 and 50 kOe depending on temperatures between 1.8 and 400 K, as well as at 2, 5, 10 and 300 K in the field regime $-50 < H < +50$ kOe. Fig. 7 shows the temperature dependence of the molar susceptibility $\chi(T) = M(T)/H$ (upper frame) for H = 10 kOe and the corresponding χT plot

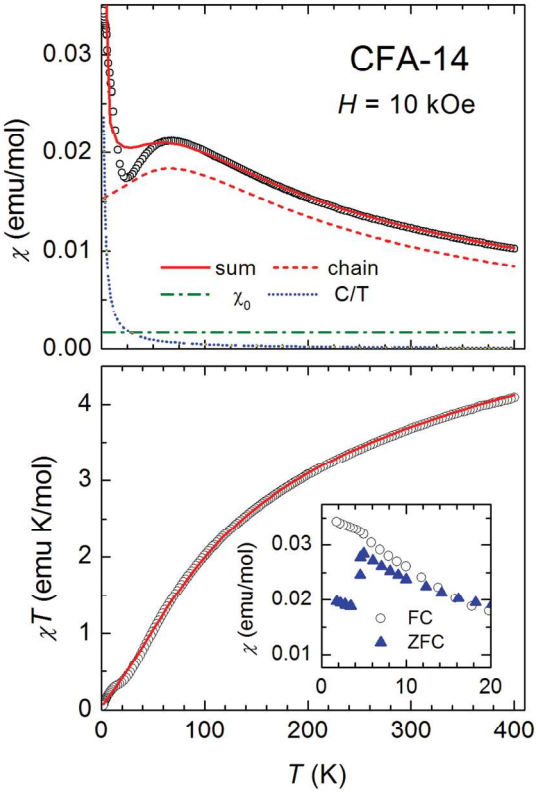

Fig. 7 Temperature-dependence of susceptibility (upper frame) and of susceptibility times temperature (lower frame) of **CFA-14** in the range of T = 1.8–400 K obtained in a magnetic field of H = 10 kOe. The fit with the linear chain model (g = 2.13, J/k_B = –18.5 K, χ_0 = 0.00173 emu mol^{-1}, and C = 0.47 emu K mol^{-1}) is shown as red solid line and the corresponding contributions as indicated in the legend. The inset in the lower frame shows the enlarged susceptibility below 20 K for field cooled (FC) and zero-field cooled (ZFC) conditions.

(lower frame). The magnetic susceptibility of **CFA-14** exhibits a maximum at about 65 K. Above this maximum the susceptibility continuously decreases with increasing temperature; for temperatures below the maximum, the susceptibility first decreases but below 20 K strongly increases again with decreasing temperature. The χT plot exhibits a monotonous decrease with decreasing temperature, which is characteristic for dominant antiferromagnetic interaction.

The field dependent magnetization is depicted in Fig. 8. As shown there, for all temperatures under consideration, the magnetization starts with a steep increase at low fields but continues approximately linearly with a clearly lower slope at higher fields. The steep increase at low fields, which persists even at room temperature, can be ascribed to small amounts of ferromagnetic impurities yielding a quickly saturating Brillouin-like contribution of the order of $10^{-2}\mu_B$ per formula unit, probably due to less than 1% cobalt clusters not detectable by X-ray diffraction. Returning to the temperature dependence of the susceptibility below 20 K, which is enlarged in the inset of the lower frame of Fig. 7, the antiferromagnetic transition can be identified by a sharp kink in the zero-field

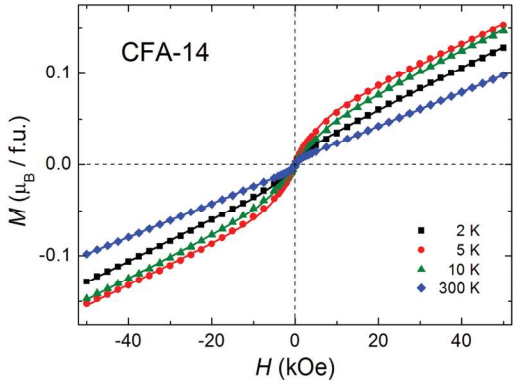

Fig. 8 Field-dependent magnetization of **CFA-14** measured at different temperatures. The solid lines represent fits by a linear term $M{\cdot}H$ plus a Brillouin function $\mu_{sat}B_{3/2}$ (H/T_{eff}) with saturation values μ_{sat} of a few $10^{-2}\mu_B$ per formula unit with effective temperatures T_{eff} < 1 K. The small effective temperatures indicate demagnetization effects in low magnetic fields.

cooled data slightly below 5 K. This is in agreement with the reduced slope of the field dependent magnetization at 2 K (with respect to the data taken at 5 K), which was also measured after zero field cooling.

For analysis of the data, we accounted for the fact that in **CFA-14** the Co^{2+} ions (with electronic configuration $3d^7$ yielding spin S = 3/2) form one-dimensional (1D) chains along the crystallographic c direction. Indeed, the temperature dependent behaviour of the magnetic susceptibility above 20 K with a maximum at about 65 K is reminiscent of the susceptibility of an antiferromagnetic linear spin chain. Therefore, the susceptibility data were analyzed in terms of a linear chain described by the Hamiltonian

$$H = -2J\sum_{i=1}^{N} S_i S_{i+1} - g\mu_B \sum_{i=1}^{N} HS_i$$

where the first term describes the exchange J between nearest neighbour spins S_i and S_{i+1} and the second term denotes the Zeeman energy in the external magnetic field H. In the classical limit the susceptibility for antiferromagnetic exchange is given by[16]

$$\chi = \frac{Ng^2{\mu_B}^2 S(S+1)}{3k_B T}\frac{1+u}{1-u}$$

$$u = \coth[2JS(S+1)/k_B T] - k_B T/2JS(S+1)$$

Using this expression plus a Curie contribution $\chi_{imp} = C/T$ of possible impurity spins and a temperature independent term χ_0 accounting for diamagnetic (<0) and temperature independent paramagnetic, *i.e.* van-Vleck (>0) contributions, we tried to fit the temperature dependence of the susceptibility. As indicated by the red solid line in the upper frame of Fig. 7, the experimental susceptibility data above 40 K can nicely be reproduced by this approach, while deviations occur at lower temperatures: the minimum at 23 K is less pronounced and the divergence of the Curie law is stronger than in the experi-

mental data. Note, however, that the classical formula for the susceptibility of the spin chain is derived from high-temperature approximation $T > J/k_B$ and, hence, cannot be expected to account for details at low temperatures. Therefore, it is satisfactory if the data are well described around the susceptibility maximum and to higher temperatures. Concerning the low-temperature Curie contribution χ_{imp}, it turned out that even introducing a Curie–Weiss temperature as a further fit parameter did not improve the fit in the low-temperature range. This means that the low-temperature increase of the susceptibility cannot be ascribed to paramagnetic impurities only, but rather seems to be intrinsic.

The description of the susceptibility data by the linear-chain model yields a g factor of 2.13 and an antiferromagnetic exchange of $J/k_B = -18.5$ K. The g value is slightly enhanced with respect to the spin-only value of 2 due to spin–orbit coupling, characteristic for ions with a more than half-filled 3d shell in the presence of tetrahedral ligand fields.[17] The temperature independent contribution of χ_0 (10 kOe) = 0.00173 emu mol^{-1} arises predominantly from the above-mentioned small amounts of ferromagnetic impurities, as evident from a comparative susceptibility measurement taken in an external field of H = 1 kOe (not shown), where the same fit yields χ_0 (1 kOe) = 0.0156 emu mol^{-1}, *i.e.* a value about 10 times larger.

To reduce the relative magnitude of the ferromagnetic contribution as much as possible, we also considered the susceptibility taken at the maximum accessible magnetic field of 50 kOe, shown in Fig. 9. Again, the temperature dependence of the susceptibility (left ordinate) is satisfactorily described by the classical one-dimensional model. Giving the temperature independent contribution free, even would yield a slightly diamagnetic contribution. Fixing $\chi_0 = 0$, we obtain a g factor of 2.15 and an antiferromagnetic exchange of $J/k_B = -16$ K. The alternative evaluation of the high-temperature data of the inverse susceptibility (right ordinate) in terms of a Curie–Weiss law ($1/\chi \sim T-\Theta$) gives a g factor of 2.17 and a Curie–Weiss temperature of $\Theta = -100$ K. The corresponding exchange constant $J/k_B = -20$ K

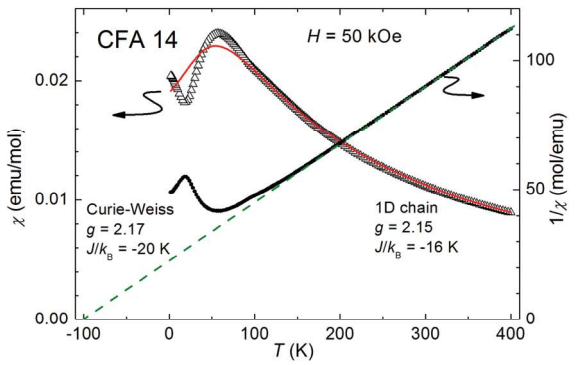

Fig. 9 Temperature-dependence of susceptibility (left ordinate) and its inverse (right ordinate) of **CFA-14** in the range of T = 1.8–400 K obtained in a magnetic field of H = 50 kOe. The fit with the linear chain model (g = 2.15, J/k_B = 16 K) is shown as red solid line, the Curie–Weiss law is indicated by a green dashed line.

is estimated from the Curie–Weiss temperature in mean-field approach $3k_B\Theta = 2ZJS(S + 1)$ with $Z = 2$ nearest neighbours, based on the spin-chain Hamiltonian above. To summarize our evaluation, we obtained average g value and exchange constant as $g = 2.15(2)$ and $J/k_B = -18(2)$ K, respectively.

Moreover, it is worth mentioning that using $\Theta = -100$ K for simultaneous evaluation of the field dependent magnetization at 300 K in Fig. 8 yields $g = 2.11$. This g value seems to be slightly smaller than the average taken from the temperature dependent susceptibilities. But this is in agreement with the observation that at high magnetic fields diamagnetism dominates all other temperature independent susceptibility contributions. Thus, the slope of the magnetization is reduced by the diamagnetic contribution implying a smaller g value.

Comparing our results to existing data in Co based MOFs similar broad maxima in the temperature dependent susceptibility have been observed in ladder structures like $Na_2Co_2(ox)_3(H_2O)_2$,[18] and are typical for quasi 1D antiferromagnets. Such a maximum indicates the onset of short range antiferromagnetic correlations within the chains, which suppress the susceptibility to lower temperatures. At first sight, the increase of the magnetic susceptibility below 25 K could be assumed to arise from spins at the chain ends or defects, which would result in a Curie-like behavior at low temperatures. However, the strong deviations of the corresponding fit from the data contradict this assumption. Regarding the onset of long range antiferromagnetic order at about T_N = 5 K the observed increase may be related to the gradual formation of long range order along the chains already above T_N. A similar temperature dependence of the susceptibility has been observed in the spin-chain compound $LiCuVO_4$.[19,20] In that material a 3D spiral spin structure is established below 2 K, but the spiral order along single chains sets in already at significantly higher temperature, which is concluded from antiferromagnetic resonance measurements, where the characteristic resonance mode can be resolved up to 12 K.[20] Indeed this coincides with the low-temperature increase of the susceptibility in $LiCuVO_4$. While in $LiCuVO_4$ magnetic frustration is responsible for the formation of the complex antiferromagnetic structure, it is possible that in **CFA-14** the chiral coupling geometry *via* OH bridges between the Co^{2+} ions induces a spiral type antiferromagnetic structure.

Photoluminescence and UV-Vis spectroscopy

Solid-state photoluminescence properties of **CFA-14** were studied at room temperature. Fig. 10 shows the photoluminescence spectrum for **CFA-14**. A broad emission band can be observed in the visible region between 350 nm and 400 nm under excitation with UV light (310 nm), while the emission of the ligand disappears.[3] The emission may be attributed to ligand-to-metal charge-transfer (LMCT) transitions. Similar LMCTs have been published for different cobalt containing MOFs and coordination polymers.[21]

The intense purple colour of the crystals is first evidence that the structure of **CFA-14** should contain tetrahedrally coordinated Co(II)-centres. In order to prove the coordination of

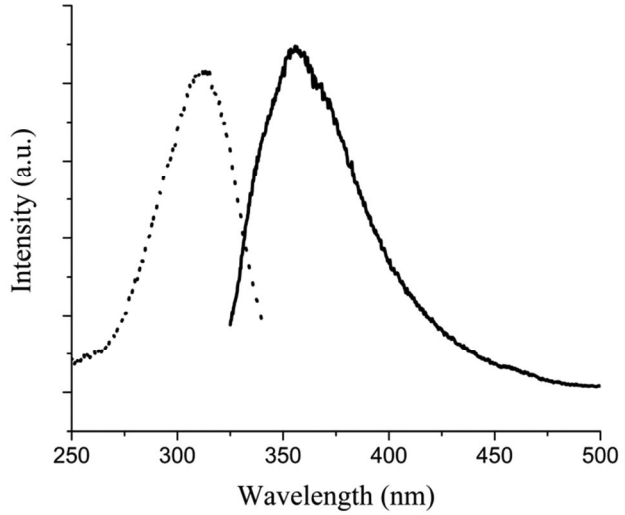

Fig. 10 Solid-state photoluminescence spectrum of **CFA-14** at room temperature. Dashed line: excitation spectrum; continuous line: emission spectrum.

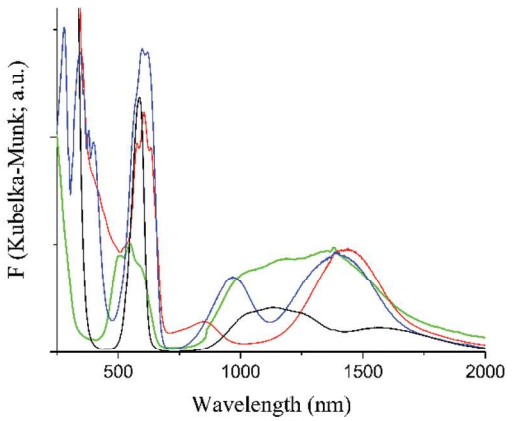

Fig. 11 UV-vis spectra of different Co-containing MOFs at room temperature: green line: **CFA-14**; black line: **MFU-2**; red line: **Co-MFU-4l**; blue line: **Co-MFU-4**.

the metal centres, **CFA-14** was analysed by solid-state UV-Vis spectroscopy (see Fig. 11, green curve). The characteristic split absorption band in the visible region centred at 550 nm results from spin-allowed d–d valence electron transition $^4A_2(F) \rightarrow {}^4T_1(P)$ of tetrahedral Co^{II} ions. The observed absorption bands correspond well to literature data of typical tetrahedral coordinated Co^{II} containing MOF compounds as apparent in the UV-Vis spectra of **MFU-2**,[5] **Co-MFU-4**[22] and **Co-MFU-4l**[23] shown in Fig. 11, which have been published by our group in earlier works.

Conclusions

This publication describes the synthesis and characterisation of the novel fluorinated metal–organic framework **CFA-14**. **CFA-14** forms an extraordinary structure containing 1-dimensional spin chains of tetrahedrally coordinated Co(II)-ions. In detail, **CFA-14** is assembled from a two-fold interpenetrated 3-D microporous structure constructed from 1-D chains of cobalt(II) ions expanding in the *c*-direction bridged by OH^- groups and $tfpb^{2-}$ ligands. The framework crystallizes in the tetragonal crystal system within the space group $I4_1/acd$ (no. 142) and exhibits strongly hydrophobic quadratic channels with apertures of 4.5 Å. **CFA-14** remains porous after solvent removal and exhibits the BET surface area of 567 $m^2\ g^{-1}$. Special features of **CFA-14** are the pronounced photoluminescence properties as well as interesting magnetic properties. SQUID measurements demonstrate that above 25 K **CFA-14** can be described as a linear chain antiferromagnet. For the lowest temperatures long range antiferromagnetism is established. We expect that a spiral type antiferromagnetic structure within **CFA-14** is potentially induced by the chiral coupling geometry *via* OH-bridges between the Co^{2+} ions. For full investigation of the magnetic structure, neutron diffraction experiments should be performed.

Experimental section

Materials and general methods

All starting materials were of analytical grade and used as obtained from commercial sources without further purification. Thermogravimetric analysis (TGA) was performed with a TGA Q500 analyser in the temperature range of 25–800 °C in a flowing nitrogen gas at a heating rate of 5 K min^{-1}. Fourier transform infrared (FTIR) spectra were recorded with an ATR unit in the range of 4000–400 cm^{-1} on a Bruker Equinox 55 FT-IR spectrometer. Diffuse reflectance infrared Fourier-transformed (DRIFT) spectra were recorded with the same instrument equipped with a Harrick Praying Mantis reaction chamber. Energy-dispersive X-ray spectroscopy (EDX) was performed with a Philips XL-30 scanning electron microscope. Variable temperature X-ray powder diffraction (VTXRPD) measurements were collected in the 2θ range of 5–60° with 0.02° steps with an Empyrean (PANalytical) Diffractometer equipped with a Bragg-Brentano^{HD} mirror, a PIXcel^{3D} 2 × 2 detector and a XRK 900 Reactor chamber (Anton Paar). The patterns were recorded in a temperature range from 25 to 400 °C, in the 5–50° 2θ range, with one step per 0.4 s, and an angular step width of 0.02° in 2θ. Temperature programme between measurements: heating rate (0.5 °C s^{-1}), then 10 min isothermal. Argon gas sorption isotherms at 77 K were measured with a Quantachrome Autosorb-I ASI-CP-8 instrument. CO_2 adsorption isotherms were measured with a BELSORP-max instrument combined with a BELCryo system. Prior to measurements, the sample was heated at 200 °C for 2 h in high vacuum to remove the occluded solvent molecules. Adsorbed gas amounts are given in $cm^3\ g^{-1}$ [STP], where STP = 101.3 kPa and 273.15 K. Luminescence spectra were acquired using a spectrofluorimeter (FS920, Edinburgh Instruments) equipped with a TMS300 monochromator, a S900 single photon photomultiplier, and a Xe 900 450 W xenon arc lamp

at r. t. The excitation and emission spectra were corrected for the wavelength-dependent lamp intensity and detector response, respectively. Magnetic susceptibility and magnetization measurements were performed using a superconducting quantum interference device (SQUID) magnetometer (Quantum Design, MPMS5) working in the temperature range of $1.8 \leq T \leq 400$ K in magnetic fields up to 5 T.

Synthesis of Co_2^{II}(tfpb)$(OH)_2$ (CFA-14)

A mixture of cobalt nitrate hexahydrate (11.6 mg; 0.04 mmol) and H_2-tfpb (9.6 mg, 0.02 mmol) was dissolved in 3 mL MeOH and 0.05 ml 2,6-lutidine and the solution was placed in a glass tube (10 mL). The tube was closed and heated at 120 °C for 3 days and then cooled to room temperature. The precipitate was filtered, washed with MeOH and dried at 100 °C under high vacuum.

Yield: 8 mg (63%). IR (ν(cm^{-1})): 3695; 1503; 1348; 1315; 1221; 1133; 1029; 998; 848; 832; 765; 740; 671; 617; 553; 507; 446. The IR-spectrum of **CFA-14** is shown in ESI (see Fig. S1†).

Single-crystal X-ray crystallography

X-ray data for the single crystal structure of **CFA-14** were collected at −173 °C on a Rigaku Saturn724 diffractometer with Si(111) channel cut monochromator using RAPID-AUTO.

The structure was solved using SHELXT and refined using SHELXL.[24] Selected crystal data and details of the structure refinement for **CFA-14** are provided in Table 1. Non-hydrogen atoms were refined with anisotropic temperature parameters. Complete crystallographic data for the structure reported in this paper have been deposited in the CIF format with the Cambridge Crystallographic Data Centre, 12 Union Road, Cambridge CB21EZ, UK as supplementary publication no. CCDC 1811523.†

Table 1 Crystal data and structure refinement of **CFA-14**

Compound	**CFA-14**
Empirical formula	$C_{16}H_6Co_2F_{12}N_4O_2$
Formula	$[Co_2(C_{16}F_{12}N_4H_4)(OH)_2]$
M_r/g mol^{-1}	632.11
T/K	100
Wavelength/Å	0.78201
Crystal system	Tetragonal
Space group	$I4_1/acd$ (no. 142)
a/Å	20.3213(11)
c/Å	12.4045(8)
V/Å^3	5122.5(6)
Z	8
D_c/g cm^{-3}	1.639
μ/mm^{-1}	1.809
F(000)	2464
θ range/°	4.370–28.082
Refls collected	16392
Refls unique	1170
R(int)	0.1739
GooF	1.210
R_1 [$I > 2\sigma(I)$]^a	0.1254
wR_2 (all data)^b	0.3677
Largest diff. peak and hole/Å^{-3}	0.940 and −0.704

^{a} $R_1 = \sum||F_o| - |F_c||/\sum|F_o|$. ^{b} $wR_2 = \sum[w(F_o^2 - F_c^2)2]/\sum[w(F_o^2)2]^{1/2}$.

Conflicts of interest

There are no conflicts to declare.

Acknowledgements

Financial support by the DFG (Priority Program SPP 1928 "COORNETs") is gratefully acknowledged. We also acknowledge partial support by the Deutsche Forschungsgemeinschaft (DFG) *via* the Transregional Collaborative Research Center TRR 80 "From Electronic Correlations to Functionality" (Augsburg, Munich, Stuttgart). We thank JASRI for the allocation of synchrotron radiation beamtime.

Notes and references

1 (*a*) C. Yang, X. Wang and M. A. Omary, *J. Am. Chem. Soc.*, 2007, **129**, 15454–15455; (*b*) C. Yang, U. Kaipa, Q. Z. Mather, X. Wang, V. Nesterov, A. F. Venero and M. A. Omary, *J. Am. Chem. Soc.*, 2011, **133**, 18094–18097; (*c*) S. Mukherjee, A. M. Kansara, D. Saha, R. Gonnade, D. Mullangi, B. Manna, A. V. Desai, S. H. Thorat, P. S. Singh, A. Mukherjee and S. K. Ghosh, *Chem. – Eur. J.*, 2016, **22**, 10937–10943; (*d*) D.-S. Zhang, Z. Chang, Y.-F. Li, Z.-Y. Jiang, Z.-H. Xuan, Y.-H. Zhang, J.-R. Li, Q. Chen, T.-L. Hu and X.-H. Bu, *Sci. Rep.*, 2013, **3**, 3312.

2 (*a*) M. Grzywa, C. Geßner, D. Denysenko, B. Bredenkötter, F. Gschwind, K. M. Fromm, W. Nitek, E. Klemm and D. Volkmer, *Dalton Trans.*, 2013, **42**, 6909–6921; (*b*) M. Grzywa, D. Denysenko, A. Schaller, A. Kalytta-Mewes and D. Volkmer, *CrystEngComm*, 2016, **18**, 7883–7893; (*c*) J.-H. Wang, M. Li and D. Li, *Chem. – Eur. J.*, 2014, **20**, 12004–12008.

3 J. Fritzsche, M. Grzywa, D. Denysenko, V. Bon, I. Senkovska, S. Kaskel and D. Volkmer, *Dalton Trans.*, 2017, **46**, 6745–6755.

4 J. Fritzsche, D. Denysenko, M. Grzywa and D. Volkmer, *Dalton Trans.*, 2017, **46**, 14907–14915.

5 M. Tonigold, Y. Lu, A. Mavrandonakis, A. Puls, R. Staudt, J. Möllmer, J. Sauer and D. Volkmer, *Chem. – Eur. J.*, 2011, **17**, 8671–8695.

6 H. Li, M. Eddaoudi, M. O'Keeffe and O. Yaghi, *Nature*, 1999, **402**, 276–279.

7 C. Heering, I. Boldog, V. Vasylyeva, J. Sanchiz and C. Janiak, *CrystEngComm*, 2013, **15**, 9757–9768.

8 A. L. Spek, *Acta Crystallogr., Sect. C: Struct. Chem.*, 2015, **71**, 9–18.

9 P.-E. Werner, L. Eriksson and M. Westdahl, *J. Appl. Crystallogr.*, 1985, **18**, 367–370.

10 P. I. Ravikovitch and A. V. Neimark, *Colloids Surf., A*, 2001, **187–188**, 11–21.

11 J. Jagiello and M. Thommes, *Carbon*, 2004, **42**, 1227–1232.
12 K. Sumida, D. L. Rogow, J. A. Mason, T. M. McDonald, E. D. Bloch, Z. R. Herm, T.-H. Bae and J. R. Long, *Chem. Rev.*, 2012, **112**(2), 724–781.
13 (*a*) A. Demessence, D. M. D'Alessandro, M. L. Foo and J. R. Long, *J. Am. Chem. Soc.*, 2009, **131**, 8784–8786; (*b*) T. M. McDonald, D. M. D'Alessandro, R. Krishna and J. R. Long, *Chem. Sci.*, 2011, **2**, 2022–2028.
14 D. Cornu, H. Guesmi, J.-M. Krafft and H. Lauron-Pernot, *J. Phys. Chem. C*, 2012, **116**, 6645–6654.
15 (*a*) J. V. Stark, D. G. Park, I. Lagadic and K. J. Klabunde, *Chem. Mater.*, 1996, **8**, 1904–1912; (*b*) A. O. Menezes, P. S. Silva, E. P. Hernández, L. E. P. Borges and M. A. Fraga, *Langmuir*, 2010, **26**(5), 3382–3387; (*c*) H. Kwon and D. G. Park, *Bull. Korean Chem. Soc.*, 2009, **30**(11), 2567–2573.
16 M. E. Fisher, *Am. J. Physiol.*, 1964, **32**, 343–346.
17 A. Abragam and B. Bleaney, *Electron Paramagnetic Resonance of Transition Ions. Clarendon Press*, Oxford, 1970.
18 M. Kurmoo, *Chem. Soc. Rev.*, 2009, **38**, 1353–1379.
19 H.-A. Krug von Nidda, L. E. Svistov, M. V. Eremin, R. M. Eremina, A. Loidl, V. Kataev, A. Validov, A. Prokofiev and W. Aßmus, *Phys. Rev. B: Condens. Matter Mater. Phys.*, 2002, **65**, 134445.
20 N. Büttgen, H.-A. Krug von Nidda, L. E. Svistov, L. A. Prozorova, A. Prokofiev and W. Aßmus, *Phys. Rev. B: Condens. Matter Mater. Phys.*, 2007, **76**, 014440.
21 (*a*) A. Abbasi, S. Tarighi and A. Badiei, *Transition Met. Chem.*, 2012, **37**, 679–685; (*b*) Z.-Y. Fu, X.-T. Wu, J.-C. Dai, S.-M. Hu, W.-X. Du, H.-H. Zhang and R.-Q. Sun, *Eur. J. Inorg. Chem.*, 2002, **10**, 2730–2735.
22 S. Biswas, M. Tonigold, M. Speldrich, P. Kögerler, M. Weil and D. Volkmer, *Inorg. Chem.*, 2010, **49**(16), 7424–7434.
23 D. Denysenko, T. Werner, M. Grzywa, A. Puls, V. Hagen, G. Eickerling, J. J. K. Reuter and D. Volkmer, *Chem. Commun.*, 2012, **48**, 1236–1238.
24 (*a*) G. M. Sheldrick, *Acta Crystallogr., Sect. A: Found. Crystallogr.*, 2008, **64**, 112; (*b*) G. M. Sheldrick, *Acta Crystallogr., Sect. C: Struct. Chem.*, 2015, **71**, 3.